Eur. J. Mineral., 36, 541–554, 2024
https://doi.org/10.5194/ejm-36-541-2024

European Journal of Mineralogy
Open Access

Fluor-rewitzerite, $[(H_2O)K]Mn_2(Al_2Ti)(PO_4)_4(OF)(H_2O)_{10} \cdot 4H_2O$, a new paulkerrite-group mineral, from the Hagendorf-Süd pegmatite, Oberpfalz, Bavaria, Germany

Rupert Hochleitner[1], Ian E. Grey[2], Anthony R. Kampf[3], Stephanie Boer[4], Colin M. MacRae[2], William G. Mumme[2], and Nicholas C. Wilson[2]

[1]Mineralogical State Collection (SNSB), Theresienstrasse 41, 80333, Munich, Germany
[2]CSIRO Mineral Resources, Private Bag 10, Clayton South, Victoria 3169, Australia
[3]Mineral Sciences Department, Natural History Museum of Los Angeles County, 900 Exposition Boulevard, Los Angeles, CA 90007, USA
[4]Australian Synchrotron, 800 Blackburn Road, Clayton, Victoria 3168, Australia

Correspondence: Ian E. Grey (ian.grey@csiro.au)

Received: 2 April 2024 – Revised: 6 May 2024 – Accepted: 8 May 2024 – Published: 26 June 2024

Abstract. Fluor-rewitzerite, $[(H_2O)K]Mn_2(Al_2Ti)(PO_4)_4(OF)(H_2O)_{10} \cdot 4H_2O$, is a new monoclinic member of the paulkerrite group, from the Hagendorf-Süd pegmatite, Oberpfalz (Upper Palatinate in English), Bavaria, Germany. It occurs on the walls of vugs in corroded zwieselite, in association with Zn- and Al-bearing earlshannonite, fluorapatite, jahnsite-(CaMnMn) and Al-rich strunzite. Fluor-rewitzerite forms clusters of colourless stubby prisms up to 0.1 mm long that are flattened on {010}; elongated along [100]; and show the forms {100}, {010}, {001}, {111} and $\{11\bar{1}\}$. Twinning occurs by 2-fold rotation about $\boldsymbol{c}$. The measured density is 2.42(2) g cm^{-3}. Optically, fluor-rewitzerite crystals are biaxial (+), with $\alpha = 1.569(3)$, $\beta = 1.582(3)$, $\gamma = 1.602(3)$ (white light) and $2V(\text{meas}) = 78(1)°$. The empirical formula from electron microprobe analyses and structure refinement is $^{A1}[(H_2O)_{0.85}K_{0.15}]_{\Sigma 1.00}{}^{A2}(K_{1.00})$ $^{M1}(Mn^{2+}{}_{1.50}Mg_{0.09}Fe^{2+}{}_{0.41})_{\Sigma 2.00}{}^{M2+M3}(Al_{1.70}Ti^{4+}{}_{0.89}Fe^{3+}{}_{0.42})_{\Sigma 3.01}(PO_4)_{3.99}{}^{X}(O_{1.09}F_{0.92})_{\Sigma 2.01}(H_2O)_{10} \cdot 4.12H_2O$. Fluor-rewitzerite has monoclinic symmetry with space group $P2_1/c$ and unit-cell parameters $a = 10.407(1)$ Å, $b = 20.514(2)$ Å, $c = 12.193(1)$ Å, $\beta = 90.49(2)°$, $V = 2603.0(4)$ Å^3 and $Z = 4$. The crystal structure was refined using synchrotron single-crystal data to $R_{\text{obs}} = 0.058$ for 6186 reflections with $I > 3\sigma(I)$. Fluor-rewitzerite is the fluoride analogue of rewitzerite, with F dominant over OH at the X sites of the general formula $A1A2M1_2M2_2M3(PO_4)_4X_2(H_2O)_{10} \cdot 4H_2O$.

1 Introduction

Rewitzerite, $[K(H_2O)]Mn_2(Al_2Ti)(PO_4)_4[O(OH)](H_2O)_{10} \cdot 4H_2O$, was recently approved as a new monoclinic mineral of the paulkerrite group (Grey et al., 2023a). The ideal formula for rewitzerite conforms to the general formula for the monoclinic group members, $A1A2M1_2M2_2M3(PO_4)_4X_2(H_2O)_{10} \cdot 4H_2O$, where $A = K$, H_2O, □ (denoting a vacancy); $M1 = Mn^{2+}$, Mg, Fe^{2+}, Zn (rarely Fe^{3+}); $M2$ and $M3 = Fe^{3+}$, Al, Ti^{4+}; and $X = O$, OH, F. A high degree of mixing of Fe^{3+}, Al and Ti^{4+} occurs at the $M2$ and $M3$ sites, and charge balance is maintained for different M^{3+}/M^{4+} ratios at $M2$ and $M3$ by variations in the X^-/X^{2-} ratios at the X sites. For end-member rewitzerite, with $M2_2M3 = Al_2Ti$, co-dominant OH^- and O^{2-} are at the X sites.

In ongoing studies of potential new secondary phosphate minerals in the Erich Keck collection at the Bavarian State Collection for Mineralogy, Munich, using scanning electron microscopy coupled with energy-dispersive X-ray analysis,

we identified a specimen as having an analysis very similar to that for rewitzerite but with more than twice the F content. More detailed studies, including electron microprobe analyses and single-crystal X-ray diffraction, confirmed the mineral as the fluoride analogue of rewitzerite with F dominant over OH at the X sites in the crystal structure. The mineral and its name have been approved by the International Mineralogical Association (IMA) Commission on New Minerals, Nomenclature and Classification (CNMNC), proposal IMA-2023-115.

The holotype specimen is housed in the mineralogical collections of the Bavarian State Mineral Collection, Munich, registration number MSM 80824. A cotype specimen used for the optical properties, powder X-ray diffraction (XRD) and Raman spectrum is located at the Natural History Museum of Los Angeles County, catalogue number 76307.

2 Occurrence and associated minerals

Fluor-rewitzerite was found in a recent study of specimens of altered zwieselite that were collected by Erich Keck in the mid-1970s from the 67 m level of the Hagendorf-Süd pegmatite mine quarry in the Oberpfalz (Upper Palatinate in English), northeast Bavaria (49°39′1″ N, 12°27′35″ E). The holotype specimen consists of altered light-brown zwieselite with many vugs up to 5 mm in diameter. The vugs are lined with tiny (< 0.1 mm) colourless crystals of fluor-rewitzerite sitting directly on the corroded zwieselite. Associated minerals are fluorapatite, white needles of Al-rich strunzite, tabular yellow crystals of Na-bearing jahnsite-(CaMnMn) and yellow microspheres of Zn- and Al-bearing earlshannonite. A massive black mineral filling some vugs has been identified by powder XRD as a Zn-bearing cryptomelane. Directly sitting on the crystals of fluor-rewitzerite are tiny white balls of iangreyite as the youngest member of the association. Directly embedded in the zwieselite and sometimes protruding into the corrosion vugs – and thus older than the fluor-rewitzerite – are massive sphalerite, tabular crystals of columbite and small grains of pyrite.

3 Physical and optical properties

Fluor-rewitzerite forms clusters of colourless stubby prisms up to 0.1 mm long (Figs. 1 and 2). The crystals are flattened on {010}; elongated along [100]; and show the forms {100}, {010}, {001}, {111} and {11$\bar{1}$} (Fig. 2). Twinning occurs by 2-fold rotation about $\boldsymbol{c}$. The density, measured by the flotation method in mixtures of methylene iodide and toluene, is 2.42(2) g cm^{-3}, compared with a value of 2.418 g cm^{-3} calculated for the empirical formula and single-crystal unit-cell parameters.

Optically, fluor-rewitzerite crystals are biaxial (+), with $\alpha = 1.569(3)$, $\beta = 1.582(3)$ and $\gamma = 1.6021(3)$ (measured in white light). The measured $2V$ from extinction data analysed with EXCALIBR (Gunter et al., 2004) is 78(1)°, and the calculated $2V$ is 78.6°. Dispersion was not observed. The optical orientation is $X = \boldsymbol{b}$, $Y = \boldsymbol{c}$ and $Z = \boldsymbol{a}$. The Gladstone–Dale compatibility index (Mandarino, 1981) is 0.035 (excellent) based on the empirical formula and the measured density.

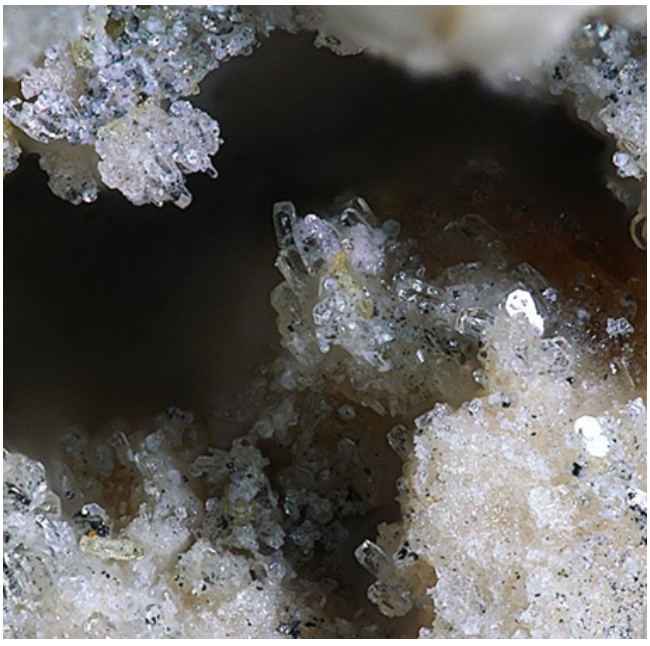

Figure 1. Fluor-rewitzerite crystals in a vug in altered zwieselite. The field of view (FOV) is 0.60 mm. Photo by Christian Rewitzer.

4 Chemical composition

Crystals of fluor-rewitzerite were analysed using wavelength-dispersive electron microprobe (EMP) spectrometry on a JEOL JXA-8530F Hyperprobe operated at an accelerating voltage of 15 kV and a beam current of 2.0 nA. The beam was defocused to between 8 and 10 µm. Both specimen and standards were coated with a 25 Å thick film of iridium for the analyses. Highly hydrated paulkerrite-group minerals present problems for analysis because of dehydration in the high vacuum of the microprobe, resulting in severe cracking and higher analytical totals (Sejkora et al., 2006). To minimise this effect, a cold stage cooled to liquid nitrogen temperature was employed in the microprobe and the specimen was precooled under dry nitrogen prior to introduction to the microprobe vacuum.

Analytical results (average of 13 analyses on four crystals) are given in Table 1. There was insufficient material for direct determination of H_2O, so it was based upon the crystal structure and stoichiometry (15 H_2O per 4 P). The calculated water content was iterated in the matrix correction procedure. The EMP results show a negative correlation between Al_2O_3 and Fe_2O_3 ($R^2 = 0.66$) and a weak positive correlation be-

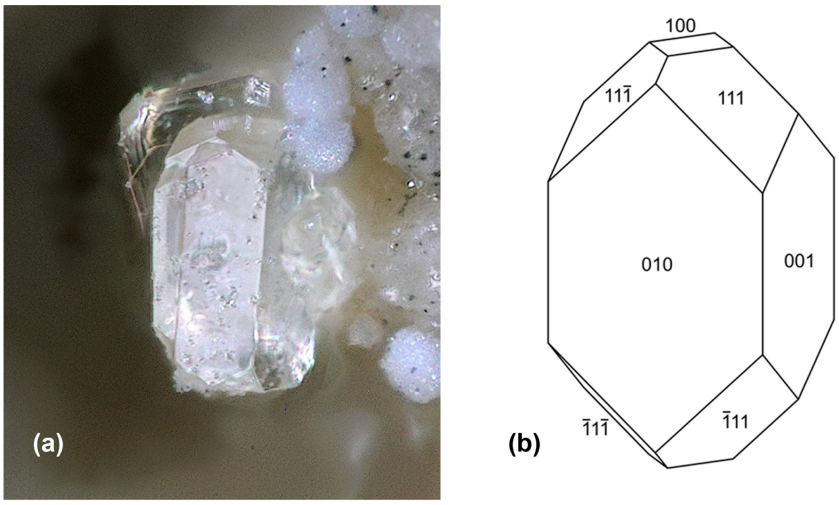

Figure 2. **(a)** Fluor-rewitzerite crystal, FOV 0.10 mm (photo Christian Rewitzer). **(b)** Crystal drawing of fluor-rewitzerite crystal.

tween Al_2O_3 and F ($R^2 = 0.40$). No significant correlations were found for K and Ti with other elements. The analysis results for rewitzerite (Grey et al., 2023a) are included in Table 1 for comparison. Fluor-rewitzerite has 50 % more K_2O than, 80 % more MnO than and more than twice the F content of rewitzerite but has lower TiO_2 and MgO contents.

The atoms per formula unit (apfu), normalised to 9($M1 + M2 + M3 + P$) apfu, are as follows:

$$K_{1.15}Mn_{1.50}Mg_{0.09}Fe^{2+}_{0.41}Fe^{3+}_{0.42}Al_{1.70}Ti^{4+}_{0.89}P_{3.99}F_{0.92}O_{32.02}H_{29.94}.$$

Expressing the apfu in structural form (general formula given in the Introduction) and grouping the $M2$ and $M3$ sites using the merged site procedure described by Grey et al. (2023b) gives the following empirical formula:

$$^{A1}[(H_2O)_{0.85}K_{0.15}]_{\Sigma 1.00}\,{}^{A2}(K_{1.00})$$
$$^{M1}(Mn^{2+}_{1.50}Mg_{0.09}Fe^{2+}_{0.41})_{\Sigma 2.00}$$
$$^{M2+M3}(Al_{1.70}Ti^{4+}_{0.89}Fe^{3+}_{0.42})_{\Sigma 3.01}\,(PO_4)_{3.99}$$
$$^{X}(O_{1.09}F_{0.92})_{\Sigma 2.01}(H_2O)_{10}\cdot 4.12H_2O.$$

The simplified formula is

$$^{A1}[(H_2O), K]^{A2}K^{M1}(Mn^{2+}, Mg, Fe^{2+})_2$$
$$^{M2+M3}(Al, Ti^{4+}, Fe^{3+})_3\,(PO_4)_4\,{}^{X}(O, F)_2\,(H_2O)_{10}\cdot 4H_2O.$$

The ideal formula is $[(H_2O)K]Mn_2(Al_2Ti)(PO_4)_4(OF)(H_2O)_{10}\cdot 4H_2O$, which requires K_2O 5.03, MnO 15.16, Al_2O_3 10.90, P_2O_5 30.34, TiO_2 8.54, F 2.03, H_2O 28.85, $-O \equiv F$ −0.85 and total 100.00 wt %.

Note that the merged ($M2_2M3$) sites approach is illustrated graphically in Fig. 4, showing a ternary Al_3–Fe^{3+}_3–Ti_3 diagram with the possible end-member compositions designated (Ti_3, Al_2Ti, Ti_2Al, etc.) and the empirical compositions for published paulkerrite-group minerals shown by crosses. The empirical ($M2_2M3$) composition for fluor-rewitzerite is shown in Fig. 4 to be located in the end-member (Al_2Ti) composition field. Combining this with the dominant species at the A, $M1$ and X sites leads to the end-member (ideal) formula reported above.

5 Raman spectroscopy

Raman spectroscopy was conducted on a Horiba XploRA PLUS spectrometer using a 532 nm diode laser, 100 µm slit, 1800 grooves mm^{-1} diffraction grating and a 100× (0.9 numerical aperture) objective. The spectrum, shown in Fig. 3, is almost identical to that for rewitzerite and the same assignments apply as given for rewitzerite (Grey et al., 2023a). The O–H stretch region has a broad peak that can be assigned to H-bonded water, with a maximum at 3355 cm^{-1} and a shoulder at 3115 cm^{-1}. Hydroxyl ion stretching is evident by a shoulder at 3570 cm^{-1}. The H–O–H bending mode region for water has a peak at 1650 cm^{-1}. Three strong peaks at 955, 970 and 1015 cm^{-1} in the P–O stretching region can be assigned to symmetric stretching modes, while weaker peaks at 1095 and 1130 cm^{-1} correspond to antisymmetric P–O stretching modes. Bending mode vibrations of the $(PO_4)^{3-}$ groups are located at 600 cm^{-1} and at 425, 445 and 480 cm^{-1}. Peaks at lower wavenumbers are related to lattice vibrations. A strong peak at 835 cm^{-1} with a shoulder at 780 cm^{-1} can be assigned to Ti–O stretch vibrations for short Ti–O bonds that occur in linear trimers of corner-connected octahedra $M2$–$M3$–$M2$ in the structure, by analogy with published Raman spectra for titanates containing short Ti–O distances (Tu et al., 1996; Bamberger et al., 1990; Silva et al., 2018).

Table 1. Analytical data (wt %) for fluor-rewitzerite.

	Fluor-rewitzerite, average of 13 analyses			Rewitzerite (Grey et al., 2023a)	
Constituent	Mean	Range	SD	Mean (SD)	Standard
K_2O	5.78	5.40–6.22	0.20	3.93 (0.61)	Adularia
MnO	11.35	9.64–12.44	0.91	6.33 (0.78)	$MnSiO_3$
MgO	0.42	0.23–0.52	0.08	2.80 (0.52)	Spinel
Al_2O_3	9.27	6.20–11.14	1.35	8.37 (1.87)	Berlinite
Fe_2O_3(total)	7.01	4.04–9.81	1.99	7.44 (1.59)	Hematite
Fe_2O_3[a]	3.54				
FeO[a]	3.11				
TiO_2	7.64	6.93–8.94	0.60	9.18 (0.77)	Rutile
P_2O_5	30.28	28.42–31.61	1.02	30.90 (2.42)	Berlinite
F	1.88	1.18–2.42	0.40	0.87 (0.31)	Fluorite
H_2O_{calc}[b]	28.80			30.39	
$-O \equiv F$	−0.79			−0.37	
Total	101.28			99.84	

[a] Based on Fe^{2+} at $M1$ and Fe^{3+} at the $M2$ and $M3$ sites. [b] Based on stoichiometry: 15 H_2O per 4 P.

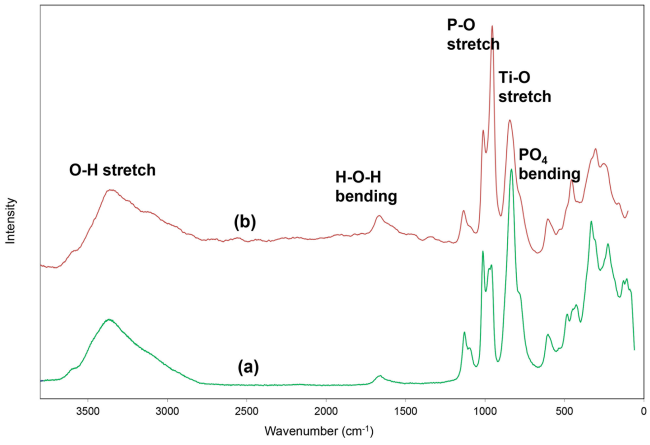

Figure 3. Raman spectrum of **(a)** fluor-rewitzerite and **(b)** rewitzerite (Grey et al., 2023a).

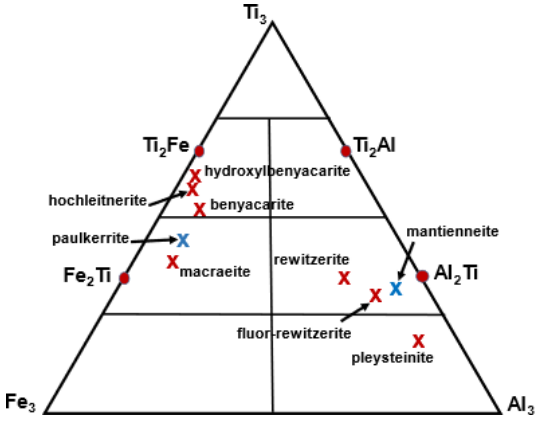

Figure 4. Ternary diagram for $(M2)_2M3$ site Al–Ti–Fe^{3+} compositions, showing end-member compositions (Al_2Ti, Ti_2Al, etc.) and location of the empirical composition for fluor-rewitzerite, For comparison the published empirical compositions are shown for the paulkerrite-group minerals benyacarite (Demartin et al., 1997), hochleitnerite (Grey et al., 2023d), hydroxylbenyacarite (Hochleitner et al., 2024), mantienneite (Fransolet et al., 1984), paulkerrite (Peacor et al., 1984), pleysteinite (Grey et al., 2023c), rewitzerite (Grey et al., 2023a) and macraeite (Grey et al., 2024). Red crosses correspond to minerals with Mn at $M1$, and blue crosses correspond to minerals with Mg at $M1$.

6 Crystallography

6.1 X-ray powder diffraction

X-ray powder diffraction data were recorded using a Rigaku R-Axis Rapid II curved-imaging-plate microdiffractometer with monochromatised Mo$K\alpha$ radiation. A Gandolfi-like motion on the ϕ and ω axes was used to randomise the sample. Observed d values and intensities were derived by profile fitting using JADE Pro software (Materials Data, Inc.). Data are given in Table 2. Refined monoclinic unit-cell parameters (space group $P2_1/c$(no. 14)) are $a = 10.425(18)$ Å, $b = 20.591(18)$ Å, $c = 12.285(18)$ Å, $\beta = 90.47(10)°$, $V = 2637(6)$ Å^3 and $Z = 4$.

6.2 Synchrotron single-crystal diffraction

A crystal measuring $0.040 \times 0.050 \times 0.070$ mm^3 was used for a single-crystal diffraction data collection at the Australian Synchrotron microfocus beamline MX2 (Aragao et al., 2018). Intensity data were collected using a Dectris Eiger 16M detector and monochromatic radiation with a wave-

Table 2. Powder X-ray diffraction data (d in Å) for fluor-rewitzerite ($I_{calc} > 1.5$).

I_{obs}	d_{obs}	d_{calc}	I_{calc}	hkl
		10.481	2	0 1 1
46	**10.256**	10.257	40	0 2 0
		9.281	2	1 1 0
62	**7.414**	7.359	57	1 1 1
		6.282	2	−1 2 1
100	**6.149**	6.096	100	0 0 2
41	**5.190**	5.203	24	2 0 0
		5.166	3	1 3 1
		5.129	11	0 4 0
17	4.659	4.640	12	2 2 0
32	3.955	3.974	5	−2 0 2
		3.913	26	2 3 1
64	**3.704**	3.733	4	−1 1 3
		3.705	21	−2 2 2
		3.680	19	2 2 2
		3.653	8	2 4 0
7	3.407	3.419	6	0 6 0
		3.319	2	−1 3 3
74	**3.119**	3.111	50	2 5 1
37	3.036	3.048	20	0 0 4
		3.025	6	−3 0 2
		3.005	6	3 0 2
24	2.962	2.982	11	0 6 2
		2.932	9	−1 0 4
80	**2.866**	2.919	11	1 0 4
		2.902	2	−3 2 2
		2.883	2	3 2 2
		2.857	32	2 6 0
14	2.812	2.819	5	−1 2 4
		2.808	5	1 2 4
		2.786	12	−1 5 3
45	**2.603**	2.639	3	−2 0 4
		2.621	4	2 0 4
		2.606	9	−3 4 2
		2.593	16	3 4 2
		2.583	3	2 6 2
		2.556	2	−2 2 4

Table 2. Continued.

I_{obs}	d_{obs}	d_{calc}	I_{calc}	hkl
34	2.519	2.545	5	−1 4 4
		2.529	10	−4 1 1
		2.521	4	4 1 1
		2.501	12	−2 7 1
		2.470	2	−3 3 3
		2.453	3	3 3 3
		2.364	2	0 8 2
20	2.323	2.337	3	−4 2 2
		2.324	2	4 2 2
		2.303	9	1 8 2
		2.275	5	0 6 4
17	2.176	2.174	6	−4 4 2
		2.163	7	4 4 2
		2.155	2	−2 8 2
7	2.095	2.089	2	−2 6 4
		2.080	2	2 6 4
		2.070	3	4 6 0
10	2.053	2.057	4	2 9 1
		2.032	8	0 0 6
29	1.972	1.987	4	−4 0 4
		1.971	3	4 0 4
		1.964	9	−4 6 2
		1.957	9	4 6 2
		1.951	2	3 8 2
		1.939	2	−5 2 2
13	1.915	1.923	2	−4 7 1
		1.910	3	1 10 2
		1.889	6	0 4 6
9	1.866	1.866	4	−2 2 6
		1.857	5	2 2 6
		1.851	2	−5 1 3
15	1.835	1.839	7	5 1 3
		1.833	2	2 8 4
		1.823	7	−2 10 2
9	1.771	1.767	2	−2 7 5
		1.760	5	−3 0 6
		1.747	5	3 0 6

Table 2. Continued.

I_{obs}	d_{obs}	d_{calc}	I_{calc}	hkl
15	1.716	1.718	2	−4 6 4
		1.710	12	0 12 0
		1.697	2	4 9 1
		1.679	2	5 7 1
28	1.653	1.664	2	−3 4 6
		1.660	3	−2 6 6
		1.653	6	2 6 6
		1.643	13	6 4 0
		1.624	3	2 12 0
18	1.600	1.611	5	4 10 0
		1.593	2	0 8 6
		1.588	6	−4 2 6
		1.583	5	6 4 2
10	1.561	1.576	3	4 2 6
		1.559	3	−4 10 2
		1.556	3	4 10 2
		1.547	3	6 6 0
6	1.511	1.525	2	−4 7 5
		1.503	4	4 11 1
		1.491	2	0 12 4
17	1.462	1.468	2	−1 11 5
		1.461	4	0 4 8
14	1.440	1.451	2	−6 4 4
		1.444	7	0 10 6
		1.437	3	6 8 0
		1.422	2	−4 11 3
		1.410	2	2 14 0
		1.393	2	−2 10 6
		1.389	2	2 10 6
		1.372	2	−3 12 4
6	1.320	1.315	3	−2 15 1
		1.311	2	4 0 8
10	1.299	1.296	2	−6 10 2
		1.292	4	−8 1 1
		1.290	2	8 1 1
		1.282	2	0 16 0

length of 0.7109 Å. The crystal was maintained at 100 K in an open-flow nitrogen cryostream during data collections. The diffraction data were collected using a single 36 s sweep of 360° rotation around ϕ. The resulting dataset consists of 3600 individual images with an approximate ϕ angle of each image being 0.1°. The raw intensity dataset was processed using XDS software to produce data files that were analysed using SHELXT (Sheldrick, 2015) and JANA2006 (Petříček et al., 2014). Refined unit-cell parameters and other data collection details are given in Table 3.

A structural model for fluor-rewitzerite was obtained in space group $P2_1/c$ using SHELXT (Sheldrick, 2015). The model had the same structure as for rewitzerite (Grey et al., 2023a), and so the rewitzerite coordinate file was used to initiate the refinement to ensure the same atom labelling. Twinning was implemented with 2-fold rotation about $\boldsymbol{c}$. Consistent with the model for rewitzerite, Mn plus Mg was incorporated at the $M1$ sites, Al and Ti at the $M2$ and $M3$ sites, and K and O (for H_2O) at the A sites, and their occupancies were refined to obtain the site scattering. Refinement of the K/O ratio at the A sites gave K occupancies lower than the K content analysed by electron microprobe (EMP). A likely explanation for this discrepancy is that the A sites also contain vacancies, as reported for other paulkerrite-group minerals (Hochleitner et al., 2024; Rewitzer et al., 2024). Adjusting the vacancy content gave a reasonable match to the EMP-derived K content for 0.1 vacancies per A site.

Difference Fourier maps were used to locate H atoms. A total of 25 H atoms were unambiguously located of a possible 30 H atoms from 15 independent H_2O groups. The H atoms were refined with soft restraints (O–H = 0.85(1) Å and H–O–H = 109.47(5)°).

Refinement with anisotropic displacement parameters for all non-H atoms and an overall isotropic parameter for Hs in JANA2006 converged at $R_{obs} = 0.058$ for 6186 reflections with $I > 3\sigma_I$. Details of the data collection and refinement are given in Table 3. The refined coordinates, equivalent isotropic displacement parameters and bond valence sum (*BVS*) values (Gagné and Hawthorne, 2015) from the refinement are reported in Table 4. Refined site scattering values are in Table 5. Anisotropic displacement parameters for the metal atoms are given in Table 6, and H bonds are reported in Table 7. Selected interatomic distances are reported in Table 8.

7 Discussion

The crystal structure for fluor-rewitzerite can be described in terms of a structural unit plus an interstitial complex, using the terminology of Hawthorne (1992) and Hawthorne and Schindler (2008). The structural unit is a 3D anionic framework of corner-connected octahedra and tetrahedra, with formula $[Mn_2Al_2Ti(PO_4)_4(OF)(H_2O)_{10}]^{1-}$, while the interstitial complex is $[K(H_2O)(H_2O)_4]^{1+}$, where the first H_2O cor-

Table 3. Crystal data and structure refinement for fluor-rewitzerite.

Ideal formula	$[(H_2O)K]Mn_2(Al_2Ti)(PO_4)_4(OF)(H_2O)_{10} \cdot 4H_2O$
Formula weight	935.7
Symmetry, space group	Monoclinic, $P2_1/c$ (#14)
Unit-cell dimensions	$a = 10.407(1)$ Å
	$b = 20.514(2)$ Å
	$c = 12.193(1)$ Å
	$\beta = 90.49(2)°$
Volume, Z	2603.0(4) Å^3, 4
Data collection	Synchrotron microfocus beamline
Wavelength, temperature	0.7109 Å, 100 K
Crystal size	$0.040 \times 0.050 \times 0.070$ mm^3
Absorption correction	Multiscan, T_{min} 0.42, T_{max} 0.75
Twinning	2-fold rotation about ***c***
	Twin volumes 0.800(3), 0.200(3)
Theta range for data collection	1.94 to 32.05°
Index ranges	$-13 \le h \le 13$, $-28 \le k \le 28$, $-16 \le l \le 16$
Reflections collected	47 535
Independent reflections	6931
Reflections with $I_o > 3\sigma(I)$	6186
Refinement method	Full-matrix least-squares method on F
Data/constraints/parameters	6931/89/477
Final R indices ($I > 3\sigma(I)$)	$R_{obs} = 0.058$, w$R_{obs} = 0.076$
R indices (all data)	$R_{obs} = 0.062$, w$R_{obs} = 0.077$
Largest diff. peak and hole	0.99 and −1.25 e Å^2

responds to transformer-type O15a, coordinated to K, and the four other H_2O groups are involved only in H bonding. These comprise O14a, O14b, O15b and *A*1 in Tables 4 and 8. The structural unit is based on (001) heteropolyhedral layers at $z = 1/4$ and 3/4, as shown in Fig. 5. The layers are built from [100] kröhnkite-type chains (Hawthorne, 1985) of four-member rings of corner-connected PO_4 tetrahedra and $M2O_4X(H_2O)$ octahedra. Each PO_4 tetrahedron also shares a corner with $M1O_2(H_2O)_4$ octahedra along [010]. The corner-shared linkages form eight-member rings of alternating octahedra and tetrahedra. Layers as shown in Fig. 5 are interconnected into an open 3D framework by corner-sharing of the $M2O_4X(H_2O)$ octahedra with $M3O_4X_2$ octahedra located at $z = 0$ and 1/2.

The interstitial complex is shown in Fig. 6. It corresponds to a (001) section through the structure centred at $z = 0$ or $z = 1/2$ with a thickness of ∼2.7 Å. In addition to the interstitial constituents and the *M*3-centred octahedra, the section contains H_2O groups that are coordinated to *M*1 cations (O10 and O12) and to *M*2 cations (O13). In-section H bonding is shown by dashed red lines on the left-hand side of Fig. 6, and in-section bonds to *A*1 and *A*2 are shown by the blue lines. Linear chains of regularly spaced water molecules, with a mean separation of ∼2.9 Å, are aligned along [110] as shown by the arrows in Fig. 6. The H bonding contributes to meeting the local bond valence requirements of undersaturated O anions shared between *M*-centred octahedra and PO_4 tetrahedra. These are O1 to O8 in Table 4.

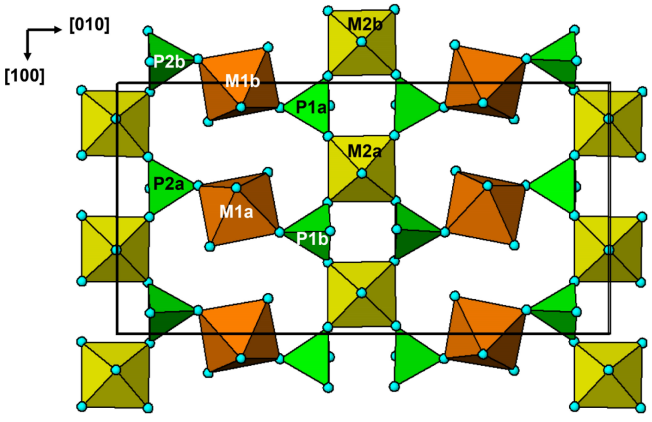

Figure 5. The (001) section through the fluor-rewitzerite crystal structure at $z = 1/4$.

Only O4a and O4b, shared between the *M*2-centred octahedra and PO_4, are not acceptors for H bonds as their valence requirements are essentially met by *M*2 and P (see *BVS* in Table 4). In addition to the H bonds to O1 to O8, there are extensive H bonds between water molecules in the interstitial complex. The strongest is from O13 to O15, with an O13···O15 distance of ∼2.7 Å, shown in Fig. 6 and in Table 7. The O13a and O13b water molecules also form H bonds with three acceptor anions. In these cases, the H points towards a face

Table 4. Refined atom coordinates, equivalent isotropic displacement parameters (Å^2) and bond valence sums (*BVS*s, in valence units) for fluor-rewitzerite.

Atom	x	y	z	U_{eq}	*BVS*
*M*1a	0.49393(4)	0.746848(17)	0.24525(3)	0.01738(16)	2.14
*M*1b	0.99657(4)	−0.246861(17)	−0.24225(3)	0.01838(16)	2.13
*M*2a	0.65985(8)	0.50245(3)	0.74352(7)	0.0192(3)	3.53
*M*2b	1.16020(7)	−0.00241(2)	−0.74189(6)	0.0195(3)	3.49
*M*3a	0.5	0.5	0.5	0.0189(4)	3.43
*M*3b	1	0	−0.5	0.0177(4)	3.46
P2a	0.58641(7)	0.58909(3)	0.29617(6)	0.01632(19)	4.98
P2b	1.08598(7)	−0.08934(3)	−0.29820(6)	0.01636(19)	4.98
P1a	0.90775(7)	0.59363(3)	0.80206(6)	0.01613(19)	4.99
P1b	1.40876(7)	−0.09344(3)	−0.80349(6)	0.01669(19)	5.00
*A*1	0.7162(2)	0.85199(9)	0.06147(17)	0.0314(7)	0.11
*A*2	1.22167(8)	−0.35426(3)	−0.05779(6)	0.0219(2)	0.85
*X*1	0.6388(2)	0.50205(7)	0.59864(17)	0.0143(5)	1.38
*X*2	1.1409(2)	−0.00368(7)	−0.59740(17)	0.0142(5)	1.34
O1a	0.9045(2)	0.66779(9)	0.80680(17)	0.0209(6)	1.74
O1b	1.4032(2)	−0.16787(9)	−0.80667(17)	0.0215(6)	1.72
O2a	1.0278(2)	0.57085(9)	0.73901(16)	0.0183(5)	1.77
O2b	1.5279(2)	−0.07012(9)	−0.73874(16)	0.0176(5)	1.75
O3a	0.90910(20)	0.56544(9)	0.91916(15)	0.0175(5)	1.82
O3b	1.4116(2)	−0.06628(9)	−0.92072(16)	0.0180(5)	1.83
O4a	0.7852(2)	0.57029(9)	0.74298(16)	0.0184(5)	1.87
O4b	1.2858(2)	−0.06974(9)	−0.74594(16)	0.0189(5)	1.99
O5a	0.5946(2)	0.66330(9)	0.29278(18)	0.0214(6)	1.71
O5b	1.0936(2)	−0.16354(9)	−0.29346(17)	0.0206(5)	1.73
O6a	0.4653(2)	0.56582(9)	0.23539(16)	0.0173(5)	1.83
O6b	0.9660(2)	−0.06573(9)	−0.23735(16)	0.0189(5)	1.85
O7a	0.5855(2)	0.56526(9)	0.41524(16)	0.0180(5)	1.84
O7b	1.0828(2)	−0.06647(9)	−0.41819(15)	0.0177(5)	1.99
O8a	0.7081(2)	0.56246(9)	0.23852(16)	0.0193(5)	1.83
O8b	1.2079(2)	−0.06239(9)	−0.24172(16)	0.0192(5)	1.83
O9a	0.3451(2)	0.68455(10)	0.17428(18)	0.0228(6)	0.39
O9b	0.8464(2)	−0.18755(10)	−0.1744(2)	0.0283(6)	0.37
O10a	0.5778(2)	0.74255(10)	0.07856(18)	0.0225(6)	0.34
O10b	1.0857(2)	−0.24137(10)	−0.07489(18)	0.0225(6)	0.46
O11a	0.6428(2)	0.80796(10)	0.31795(18)	0.0226(6)	0.35
O11b	1.1473(2)	−0.30809(10)	−0.3057(2)	0.0275(6)	0.40
O12a	0.3979(2)	0.75123(10)	0.40594(18)	0.0236(6)	0.44
O12b	0.9027(2)	−0.25309(10)	−0.40946(18)	0.0236(6)	0.31
O13a	0.6655(2)	0.50409(8)	0.9115(2)	0.0212(6)	0.43
O13b	1.1632(3)	−0.00056(8)	−0.9124(2)	0.0245(7)	0.40
O14a	0.2586(2)	0.63984(10)	0.44014(17)	0.0255(6)	0
O14b	0.7592(2)	−0.14199(10)	−0.43957(17)	0.0241(6)	0
O15a	0.5418(2)	0.41004(11)	1.0177(2)	0.0292(7)	0.15
O15b	1.0197(3)	0.09405(13)	−1.00606(18)	0.0335(8)	0.01
H9a1	0.263(2)	0.6824(19)	0.183(4)	0.049(3)	
H9a2	0.379(3)	0.6486(15)	0.191(4)	0.049(3)	
H9b1	0.769(3)	−0.188(3)	−0.199(4)	0.049(3)	
H10a2	0.621(4)	0.7119(18)	0.052(4)	0.049(3)	
H10b1	1.018(3)	−0.2505(19)	−0.042(3)	0.049(3)	
H10b2	1.122(4)	−0.2087(17)	−0.044(3)	0.049(3)	
H11a1	0.721(2)	0.804(2)	0.320(4)	0.049(3)	
H11a2	0.624(4)	0.8446(15)	0.292(4)	0.049(3)	
H11b1	1.232(2)	−0.3136(19)	−0.302(4)	0.049(3)	
H11b2	1.111(3)	−0.3442(14)	−0.301(4)	0.049(3)	

Table 4. Continued.

Atom	x	y	z	U_{eq}
H12a1	0.467(3)	0.7468(17)	0.439(4)	0.049(3)
H12a2	0.359(4)	0.7142(14)	0.403(4)	0.049(3)
H12b1	0.856(4)	−0.2208(17)	−0.415(4)	0.049(3)
H13a1	0.627(4)	0.4714(18)	0.938(3)	0.049(3)
H13a2	0.737(3)	0.5089(18)	0.944(4)	0.049(3)
H13b1	1.223(4)	0.0022(18)	−0.960(3)	0.049(3)
H13b2	1.097(3)	0.019(2)	−0.936(3)	0.049(3)
H14a1	0.310(4)	0.6195(19)	0.483(3)	0.049(3)
H14a2	0.245(4)	0.6179(17)	0.386(3)	0.049(3)
H14b1	0.751(4)	−0.1178(16)	−0.385(2)	0.049(3)
H14b2	0.796(4)	−0.1202(17)	−0.492(3)	0.049(3)
H15a1	0.468(3)	0.405(3)	0.987(4)	0.049(3)
H15b1	0.948(3)	0.089(2)	−0.976(3)	0.049(3)
H15b2	1.018(3)	0.078(2)	−1.070(2)	0.049(3)
Ha1a	0.685(5)	0.877(2)	0.014(4)	0.049(3)

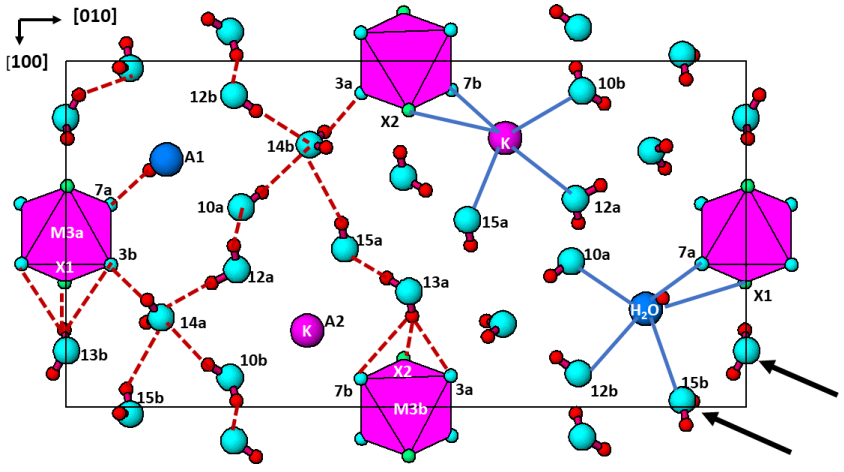

Figure 6. The (001) section through the fluor-rewitzerite structure at $z = 0$. Dashed red lines on the left-hand side of the figure show H bonds, and solid blue lines on the right-hand side show bonding associated with the $A1$ and $A2$ sites. Arrows show [110] rows of regularly spaced H_2O groups.

Table 5. Refined site scattering for fluor-rewitzerite.

Site	Scattering used in refinement*	Scattering (electrons)
$M1$a	0.940(7) Mn + 0.060 Mg	24.2
$M1$b	0.946(8) Mn + 0.054 Mg	24.3
$M2$a	0.593(12) Al + 0.407 Ti	16.7
$M2$b	0.476(12) Al + 0.524 Ti	17.7
$M3$a	0.753(15) Al + 0.247 Ti	15.2
$M3$b	0.685(15) Al + 0.315 Ti	15.8
$A1$	0.130(7) K + 0.770(7) O + 0.1 □	8.6
$A2$	0.887(6) K + 0.013 O + 0.1 □	17.0

* Mn scattering curve used for Mn plus minor Fe; Ti scattering curve used for Ti plus minor Fe.

X–O3–O7 of an $M3$-centred octahedron and forms H bonds with all three anions forming the face as shown in Fig. 6.

The major difference between the crystal structure of fluor-rewitzerite and that of the orthorhombic paulkerrite-group mineral benyacarite (Demartin et al., 1993) is an ordering of K and H_2O at the $A1$ and $A2$ sites, whereas they are disordered at a single A site in benyacarite. It would be expected that the ordering of the positive K^+ cation at a specific A site would be associated with a localised negative charge at the associated structural unit site. For the ideal end-member fluor-rewitzerite with a structural unit formula of $[Mn_2Al_2Ti(PO_4)_4(OF)(H_2O)_{10}]^{1-}$, the local $M2$–X–$M3$-ordered groupings in the structural unit will be predominantly Al–F–Al and Al–O–Ti. The first is formally charge-balanced for octahedrally coordinated Al, but the latter will give rise to an undersaturated bridging O^{2-} anion. It would

Table 6. Anisotropic displacement parameters (Å^2) for metal atom sites in fluor-rewitzerite.

	U^{11}	U^{22}	U^{33}	U^{12}	U^{13}	U^{23}
*M*1a	0.0214(3)	0.0096(2)	0.0212(3)	0.00151(15)	0.00041(17)	0.00117(14)
*M*1b	0.0220(3)	0.0100(2)	0.0232(3)	−0.00056(15)	0.00029(17)	0.00246(14)
*M*2a	0.0190(5)	0.0090(4)	0.0295(5)	−0.00007(18)	−0.0012(3)	−0.00008(18)
*M*2b	0.0212(5)	0.0090(4)	0.0283(4)	−0.00042(17)	0.0014(3)	−0.00075(17)
*M*3a	0.0255(8)	0.0110(6)	0.0200(6)	0.0000(3)	0.0024(4)	0.0001(3)
*M*3b	0.0242(7)	0.0104(5)	0.0185(6)	−0.0003(3)	−0.0011(4)	−0.0001(3)
P1a	0.0211(4)	0.0092(3)	0.0181(3)	−0.0001(2)	0.0007(2)	0.0016(2)
P1b	0.0213(4)	0.0094(3)	0.0193(3)	−0.0002(2)	−0.0001(2)	0.0012(2)
P2a	0.0208(4)	0.0089(3)	0.0192(3)	−0.0001(2)	0.0000(2)	0.0010(2)
P2b	0.0214(4)	0.0090(3)	0.0187(3)	0.0001(2)	0.0004(2)	0.0019(2)
*A*1	0.0476(15)	0.0153(10)	0.0314(12)	0.0043(7)	−0.0027(8)	−0.0014(6)
*A*2	0.0279(4)	0.0139(3)	0.0238(4)	−0.0003(2)	0.0026(2)	0.0018(2)

Table 7. Hydrogen bonding in fluor-rewitzerite.

D–H···*A*	*D*–H (Å)	H···*A* (Å)	*D*···*A* (Å)	∠*DHA* (°)
O9a–H9a1···O5b	0.86(3)	1.83(3)	2.684(3)	170(4)
O9a–H9a2···O6a	0.84(3)	1.99(3)	2.835(3)	177(4)
O9b–H9b1···O5a	0.85(3)	1.89(3)	2.694(3)	157(5)
O10a–H10a2···O14b	0.84(4)	2.03(4)	2.807(3)	153(4)
O10b–H10b1···O12b	0.84(3)	2.02(4)	2.787(3)	153(4)
O10b–H10b2···O14a	0.86(4)	2.01(4)	2.758(3)	145(4)
O11a–H11a1···O1a	0.82(3)	2.01(3)	2.773(3)	156(4)
O11a–H11a2···O2b	0.83(3)	2.05(3)	2.854(3)	161(4)
O11a–H11a2···O4a	0.83(3)	2.50(4)	3.048(3)	125(3)
O11b–H11b1···O1b	0.89(3)	1.82(3)	2.709(3)	173(5)
O11b–H11b2···O2a	0.83(3)	2.01(3)	2.832(3)	170(5)
O12a–H12a1···O10a	0.83(4)	2.06(4)	2.809(3)	150(4)
O12a–H12a2···O14a	0.86(3)	1.91(3)	2.740(3)	162(4)
O12b–H12b1···O14b	0.82(4)	1.93(4)	2.748(3)	174(4)
O13a–H13a1···O15a	0.85(4)	1.82(4)	2.661(3)	170(4)
O13a–H13a2···X2	0.84(4)	2.27(4)	3.025(3)	149(4)
O13a–H13a2···O3a	0.84(4)	2.16(4)	2.831(3)	137(4)
O13a–H13a2···O7b	0.84(4)	2.45(4)	2.993(3)	123(3)
O13b–H13b1···X1	0.86(4)	2.23(4)	3.079(4)	173(4)
O13b–H13b1···O3b	0.86(4)	2.46(4)	2.918(3)	114(3)
O13b–H13b1···O7a	0.86(4)	2.43(4)	2.944(3)	119(3)
O13b–H13b2···O15b	0.85(4)	1.93(4)	2.697(3)	150(4)
O14a–H14a1···O3b	0.85(4)	1.92(4)	2.766(3)	174(4)
O14a–H14a2···O8b	0.81(3)	1.96(3)	2.775(3)	177(4)
O14b–H14b1···O8a	0.84(3)	1.94(3)	2.771(3)	172(4)
O14b–H14b2···O3a	0.87(3)	1.96(4)	2.812(3)	165(3)
O15b–H15b1···O14a	0.84(3)	2.44(3)	3.155(4)	144(4)
O15b–H15b2···O2a	0.84(3)	2.12(3)	2.918(3)	159(4)
A1–Ha1a···O7a	0.84(5)	1.97(5)	2.806(3)	171(5)

be expected that the K^+ would be associated with this configuration, and this appears to be borne out by the results in Tables 5 and 8. The K at the *A*2 site is coordinated to *X*2, which is shared between *M*2b containing dominant Ti and *M*3b containing dominant Al, whereas H_2O at the *X*1 site is associated with *M*2a and *M*3a, both containing dominant Al. This ordering should be manifested in *X*2 being predominantly O^{2-} and *X*1 being predominantly F^-, but the *BVS* values in Table 4 do not reflect this. However, the *BVS* values for *X*1 and *X*2 are calculated from the mean positions of cations at the *M*2 and *M*3 sites, whereas these sites contain different cations, Al^{3+}, Fe^{3+} and Ti^{4+}, which may each be

Table 8. Polyhedral bond lengths [Å] for fluor-rewitzerite.

*M*1a–O1b	2.084(2)	*M*1b–O1a	2.086(2)
–O5a	2.088(2)	–O5b	2.081(2)
–O9a	2.178(2)	–O9b	2.153(2)
–O10a	2.221(2)	–O10b	2.238(2)
–O11a	2.178(2)	–O11b	2.159(2)
–O12a	2.208(2)	–O12b	2.257(2)
Avg.	2.159	Avg.	2.163
*M*2a–*X*1	1.777(2)	*M*2b–*X*2	1.774(2)
–O2b	1.966(2)	–O2a	1.978(2)
–O4a	1.906(2)	–O4b	1.904(2)
–O6a	1.929(2)	–O6b	1.934(2)
–O8b	1.915(2)	–O8a	1.911(2)
–O13a	2.050(3)	–O13b	2.079(3)
Avg.	1.924	Avg.	1.930
*M*3a–*X*1 x2	1.873(2)	*M*3b–*X*2 x2	1.897(2)
–O3b x2	1.913(2)	–O3a x2	1.909(2)
–O7a x2	1.915(2)	–O7b x2	1.892(2)
Avg.	1.900	Avg.	1.899
P1a–O1a	1.523(2)	P1b–O1b	1.529(2)
–O2a	1.545(2)	–O2b	1.540(2)
–O3a	1.542(2)	–O3b	1.530(2)
–O4a	1.539(2)	–O4b	1.540(2)
Avg.	1.537	Avg.	1.535
P2a–O5a	1.525(2)	P2b–O5b	1.528(2)
–O6a	1.534(2)	–O6b	1.535(2)
–O7a	1.533(2)	–O7b	1.537(2)
–O8a	1.553(2)	–O8b	1.541(2)
Avg.	1.536	Avg.	1.535
*A*1–*X*1	3.132(2)	*A*2–*X*2	3.070(2)
–O4a	2.815(3)	–O4b	2.858(2)
–O7a	2.801(3)	–O7b	2.771(2)
–O9b	3.293(3)	–O9a	3.200(2)
–O10a	2.673(3)	–O10b	2.720(2)
–O11a	3.350(3)	–O11b	3.251(3)
–O12b	2.835(3)	–O12a	2.836(2)
–O15b	3.056(3)	–O15a	2.754(3)
Avg.	2.994	Avg.	2.933

at different positions in the octahedra. The anisotropic displacement parameters (ADPs) for the *M*2 sites in Table 6 show elevated values for U^{33}, corresponding to root-mean-square displacements of 0.17 Å. Displacements of individual cations by this magnitude will have large effects on the *BVS* values for the *X* sites. We tried refining the O/F contents at these sites, but these anions are isoelectronic and the refinements were inconclusive. We also tried refinements in the non-centrosymmetric space group *Pc*, but the refinements were unstable (oscillating) and gave non-positive ADPs and large ranges for the P–O distances.

There are currently nine published paulkerrite-group minerals, which are distinguished compositionally in Fig. 4. The first three members to be characterised, paulkerrite (Peacor et al., 1984), mantienneite (Fransolet et al., 1984) and benyacarite (Demartin et al., 1993, 1997), were all described as having orthorhombic symmetry, space group *Pbca*, and this appeared to be confirmed from a single-crystal refinement for benyacarite. The new members pleysteinite and hochleitnerite (Grey et al., 2023c, d) were reported to be isostructural with benyacarite, based on laboratory-based single-crystal diffraction data. A single-crystal study on type paulkerrite using microfocus synchrotron diffraction data, however, revealed a small monoclinic distortion of the published unit cell ($\beta = 90.33(3)°$) with the crystal structure conforming to $P2_1/c$, a maximum non-isomorphous subgroup of *Pbca* (Grey et al., 2023b). Peacor et al. (1984) had already noted the poor diffracting quality of paulkerrite crystals and the "possibility of submicroscopic domains having a structure differing from the average". We subsequently collected microfocus synchrotron diffraction data on crystals of pleysteinite and hochleitnerite and confirmed that these minerals are also monoclinic, $P2_1/c$ (Rewitzer et al., 2024). The combination of a very small deviation of β from 90°, ubiquitous twinning and large mosaicity makes it difficult to determine the correct symmetry using conventional sealed-tube laboratory diffractometer data. Recent microfocus synchrotron data collected on the new paulkerrite-group minerals, rewitzerite (Grey et al., 2023a), hydroxylbenyacarite (Hochleitner et al., 2024) and macraeite (Grey et al., 2024), have confirmed the monoclinic character of these minerals. It is likely that the crystal structure of benyacarite is also of monoclinic symmetry. An indication of this comes from the very large displacement parameters reported for O15 (Demartin et al., 1993), with $U \sim 0.05$ Å^2 corresponding to a mean-square displacement of 0.22 Å. In going from the average *Pbca* structure to $P2_1/c$, the largest displacements occur for O15 in published monoclinic structures (Rewitzer et al., 2024). This is shown for fluor-rewitzerite in Table 8, where *A*1–O15b and *A*2–O15a distances differ by 0.30 Å, whereas all the other pairs of *A*–O distances differ by less than 0.1 Å. The large *U* values for O15 from the *Pbca* refinement of benyacarite thus suggest that the correct symmetry is monoclinic, at least in small domains.

Some trends in the crystal chemistry of the seven monoclinic paulkerrite-group minerals are given in Table 9. The magnitude of the monoclinic distortion correlates positively with the difference in scattering between the *A*1 and *A*2 sites, that is, with the extent of ordering of K and H_2O at the *A* sites. This is illustrated in Fig. 7 ($R^2 = 0.70$). There is a correlation between the monoclinicity and the extent of twinning. The minerals with the greatest monoclinicity are untwinned or have a dominant twin individual, and decreasing monoclinicity is associated with a shift towards equal twin volumes. Also given in Table 9 is information on the reflections $(hk0)$, $h = 2n + 1$, and $(0kl)$, $k = 2n + 1$. These

Table 9. Crystal–chemical trends in monoclinic paulkerrite-group minerals, general formula $A1A2M1_2M2_2M3(PO_4)_4X_2(H_2O)_{10}\cdot 4H_2O$.

	Pleysteinite	Fluor-rewitzerite	Paulkerrite	Rewitzerite	Macraeite	Hochleitnerite	Hydroxyl-benyacarite
A1, *A2*, *M*1, ($M2_2M3$), X_2	H_2O, K, Mn, (Al_3), F_2	H_2O, K, Mn, (Al_2Ti), OF	H_2O, K, Mg, (Fe_2Ti), OF	K, H_2O, Mn, (Al_2Ti), O(OH)	H_2O, K, Mn, (Fe_2Ti), O(OH)	H_2O, K, Mn, (Ti_2Fe), O_2	H_2O, H_2O, Mn, Ti_2Fe, (O(OH)
K_2O (wt %)	5.20	5.78	5.15	3.93	4.14	4.64	2.25
TiO_2 (wt %)	5.47	7.64	10.85	9.18	9.85	12.95	14.57
Al_2O_3 (wt %)	12.14	9.27	1.29	8.37	1.65	0.64	0.08
Fe_2O_3 (wt %)	1.72	3.54	12.66	7.44	11.80	9.78	9.98
F (wt %)	2.41	1.88	0.99	0.87	1.04	0.44	0.32
a (Å) *b* (Å) *c* (Å) *β* (°)	10.440(5) 20.588(5) 12.234(2) 90.38(1)°	10.407(1) 20.514(2) 12.193(1) 90.49(2)	10.569(2) 20.590(4) 12.413(2) 90.33(3)°	10.442(2) 20.445(2) 12.269(1) 90.17(3)°	10.562(2) 20.725(4) 12.416(2) 90.09(3)°	10.547(2) 20.577(4) 12.373(2) 90.09(3)°	10.5467(3) 20.7222(5) 12.5031(3) 90.068(2)
Twin volumes	0.91, 0.09	0.80, 0.20	No twinning	0.62, 0.38	0.63, 0.37	0.55, 0.45	0.51, 0.49
Site scattering *A*1, *A*2 (electrons)	18.2, 7.7	17.1, 8.9	15.6, 8.7	15.7, 8.3	15.2, 9.9	12.8, 8.5	9.8, 7.7
*Observed, all, R_p $hk0$, $h = 2n+1$	85, 173, 0.12	112, 152, 0.10	40, 168, 0.19	101, 130, 0.08	87, 119, 0.13	66, 146, 0.16	55, 143, 0.28
$0kl$, $k = 2n+1$	104, 185, 0.12	92, 106, 0.14	37, 188, 0.17	100, 121, 0.11	94, 136, 0.13	94, 160, 0.15	75, 200, 0.28

* Reflections forbidden in *Pbca*.

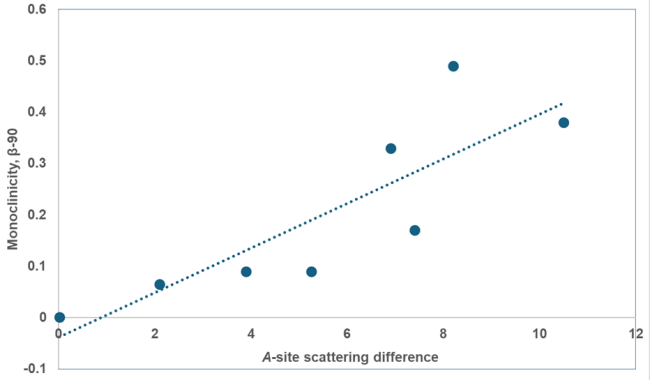

Figure 7. Plot of *A*-site scattering difference vs. β-90 (°) for monoclinic paulkerrite-group minerals.

reflections are systematically absent in the diffraction patterns of the orthorhombic *Pbca* minerals due to the *a* and *b* glide planes. Their presence, as well as their fitting in the refinement, is the most direct evidence for the space group $P2_1/c$. The results for paulkerrite appear to be anomalous, with much lower numbers of these reflections, but this is because the reflection data are much weaker, with only 40 % of reflections having $I > 3\sigma(I)$ (Grey et al., 2023b) compared with ∼ 90 % for the other minerals. Aside from paulkerrite, there is a general trend from left to right (direction of decreasing monoclinicity and K/H_2O ordering) of smaller numbers of observed "forbidden" reflections and increasing partial *R* factors (R_p) in the fitting of these reflections. Hydroxylbenyacarite, which has only about half the K content of the other minerals, is the most extreme in terms of the smallest monoclinicity and *A*-site scattering difference, and it has the poorest fit to the forbidden reflection intensities. Reconstructed precession images of the diffraction data for this mineral show that the reflections ($hk0$), $h = 2n+1$, and ($0kl$), $k = 2n+1$, are diffuse with streaking parallel to $\boldsymbol{b}^*$ (Hochleitner et al., 2024). The lengths of the diffuse streaks correspond to correlation lengths of only 1 to 2 nm, so the *A*-site ordering is restricted to domains on the scale of the unit cell. The results in Table 9 are consistent with a progressive decease in the size of the domains in which ordering of K and H_2O at the *A* sites occurs, in the minerals from left to right in the table.

The general crystallographic trends shown in Table 9 correlate strongly with the mineral compositions. In particular, the decrease in *A* site scattering and associated smaller monoclinicity from left to right in Table 9 are associated with decreases in K, Al and F and with increases in Ti content. The variation in Fe^{3+} is less clear, but overall it increases from left to right, with the clear exception of paulkerrite. The elements Al, Fe^{3+}, Ti and F are all associated with the octahedra at the $M2_2M3$ sites, suggesting that it is the distribution of compositions at these sites that determines the extent of monoclinic ordering. Figure 4 shows a distinct difference in the compositions of minerals that have Al > Fe at the $M2_2M3$ sites compared with those that have Fe > Al. The former all have $M2_2M3$ compositions in the range of M_2^{3+}Ti

to M_3^{3+} (M^{3+}-rich), whereas the latter have compositions in the range of M_2^{3+}Ti to $M^{3+}Ti_2$ (Ti-rich). Minerals in the Al-rich Al_3 and Al_2Ti phase fields (pleysteinite, fluor-rewitzerite and rewitzerite) have the highest degree of monoclinic ordering, whereas minerals in the Ti-rich Ti_2Fe phase field have the lowest degree of ordering (hydroxylbenyacarite, hochleitnerite and benyacarite). The mineral mantienneite remains unclassified because the crystals are not of high-enough quality for a single-crystal structure determination. At present there are no known paulkerrite-group minerals with $M2_2M_3$ compositions in the Fe_3 or Ti_2Al phase fields. Eventual discovery and characterisation of minerals in these two phase fields will help to further develop an understanding of the factors that determine the monoclinic ordering.

Data availability. Crystallographic data for fluor-rewitzerite are available in the Supplement.

Supplement. The supplement related to this article is available online at: https://doi.org/10.5194/ejm-36-541-2024-supplement.

Author contributions. IEG oversaw the research and wrote the paper; RH conducted initial characterisation studies on the specimen and identified it as a potential new species; WGM assisted in the diffraction data analysis; ARK measured the optical properties, Raman spectrum, powder XRD and crystal morphology; SB collected and processed the single-crystal diffraction data; and NCW and CMM developed the cryo-EMP analysis procedure and associated software.

Competing interests. The contact author has declared that none of the authors has any competing interests.

Disclaimer. Publisher's note: Copernicus Publications remains neutral with regard to jurisdictional claims made in the text, published maps, institutional affiliations, or any other geographical representation in this paper. While Copernicus Publications makes every effort to include appropriate place names, the final responsibility lies with the authors.

Acknowledgements. We thank Cameron Davidson for preparing polished mounts for EMP analyses. This research was undertaken in part using the MX2 beamline at the Australian Synchrotron, part of ANSTO, and made use of the Australian Cancer Research Foundation detector.

Review statement. This paper was edited by Sergey Krivovichev and reviewed by Gennaro Ventruti and one anonymous referee.

References

Aragao, D., Aishima, J., Cherukuvada, H., Clarken, R., Clift, M., Cowieson, N. P., Ericsson, D. J., Gee, C. L., Macedo, S., Mudie, N., Panjikar, S., Price, J. R., Riboldi-Tunnicliffe, A., Rostan, R., Williamson, R., and Caradoc-Davies, T. T.: MX2: a high-flux undulator microfocus beamline serving both the chemical and macromolecular crystallography communities at the Australian Synchrotron, J. Synch. Radiat., 25, 885–891, 2018.

Bamberger, C. E., Begun, G. M., and MacDougall, C. S.: Raman spectroscopy of potassium titanates: Their synthesis, hydrolytic reactions and thermal stability, Appl. Spectrosc., 44, 31–37, 1990.

Demartin, F., Pilati, T., Gay, H. D., and Gramaccioli, C. M.: The crystal structure of a mineral related to paulkerrite, Z. Kristallogr., 208, 57–71, 1993.

Demartin, F., Gay, H. D., Gramaccioli, C. M., and Pilati, T.: Benyacarite, a new titanium-bearing phosphate mineral species from Cerro Blanco, Argentina, Can. Mineral., 35, 707–712, 1997.

Fransolet, A.-M., Oustriere, P., Fontan, F., and Pillard, F.: La mantiennéite, une novelle espèce minérale du gisement de vivianite d'Anloua, Cameroun, B. Mineral., 107, 737–744, 1984.

Gagné, O. C. and Hawthorne, F. C.: Comprehensive derivation of bond-valence parameters for ion pairs involving oxygen, Acta Crystallogr. B, 71, 562–578, 2015.

Grey, I. E., Hochleitner, R., Kampf, A. R., Boer, S., MacRae, C. M., Mumme, W. G., and Keck, E.: Rewitzerite, $[K(H_2O)]Mn_2(Al_2Ti)(PO_4)_4[O(OH)](H_2O)_{10}\cdot 4H_2O$, a new monoclinic paulkerrite-group mineral, from the Hagendorf Süd pegmatite, Oberpfalz, Bavaria, Germany, Mineral. Mag., 87, 830–838, 2023a.

Grey, I. E., Boer, S., MacRae, C. M., Wilson, N. C., Mumme, W. G., and Bosi, F.: Crystal chemistry of type paulkerrite and establishment of the paulkerrite group nomenclature, Eur. J. Mineral., 35, 909–919, 2023b.

Grey, I. E., Hochleitner, R., Rewitzer, C., Kampf, A. R., MacRae, C. M., Gable, R. W., Mumme, W. G., Keck, E., and Davidson, C.: Pleysteinite, $[(H_2O)_{0.5}K_{0.5}]_2Mn_2Al_3(PO_4)_4F_2(H_2O)_{10}\cdot 4H_2O$, the Al analogue of benyacarite, from the Hagendorf Süd pegmatite, Oberpfalz, Bavaria, Germany, Eur. J. Mineral., 35, 189–197, 2023c.

Grey, I. E., Keck, E., Kampf, A. R., MacRae, C. M., Gable, R. W., Mumme, W. G., Glenn, A. M., and Davidson, C.: Hochleitnerite, $[K(H_2O)]Mn_2(Ti_2Fe)(PO_4)_4O_2(H_2O)_{10}\cdot 4H_2O$, a new paulkerrite-group mineral, from the Hagendorf-Süd pegmatite, Oberpfalz, Bavaria, Germany, Eur. J. Mineral., 35, 635–643, 2023d.

Grey, I. E., Rewitzer, C., Hochleitner, R., Kampf, A. R., Boer, S., Mumme, W. G., and Wilson, N. C.: Macraeite, $[(H_2O)K]Mn_2(Fe_2Ti)(PO_4)_4[O(OH)](H_2O)_{10}\cdot 4H_2O$, a new monoclinic paulkerrite-group mineral, from the Cubos-Mesquitela-Mangualde pegmatite, Portugal, Eur. J. Mineral., 36, 267–278, 2024.

Gunter, M. E., Bandli, B. R., Bloss, F. D., Evans, S. H., Su, S. C., and Weaver, R.: Results from a McCrone spindle stage short course, a new version of EXCALIBR, and how to build a spindle stage, Microscope, 52, 23–39, 2004.

Hawthorne, F. C.: Towards a structural classification of minerals: The $^{vi}M^{iv}T_2\Phi_n$ minerals, Am. Mineral., 70, 455–473, 1985.

Hawthorne, F. C.: The role of OH and H_2O in oxide and oxysalt minerals, Z. Kristallogr., 201, 41–68, 1992.

Hawthorne, F. C. and Schindler, M.: Understanding the weakly bonded constituents in oxysalt minerals, Z. Kristallogr., 223, 183–206, 2008.

Hochleitner, R., Rewitzer, C., Grey, I. E., Kampf, A. R., MacRae, C. M., Gable, R. W., and Mumme, W. G.: Hydroxylbenyacarite, $(H_2O)_2Mn_2(Ti_2Fe)(PO_4)_4[O(OH)](H_2O)_{10} \cdot 4H_2O$, a new paulkerrite-group mineral from the El Criollo mine, Cordoba province, Argentina, Mineral. Mag., https://doi.org/10.1180/mgm.2024.16, online first, 2024.

Mandarino, J. A.: The Gladstone-Dale relationship: Part IV. The compatibility concept and its application, Can. Mineral., 19, 441–450, 1981.

Peacor, D. R., Dunn, P. J., and Simmons, W. B.: Paulkerrite a new titanium phosphate from Arizona, Mineral. Rec., 15, 303–306, 1984.

Petříček, V., Dušek, M., and Palatinus, L.: Crystallographic Computing System JANA2006: General features, Z. Kristallogr., 229, 345–352, 2014.

Rewitzer, C., Hochleitner, R., Grey, I. E., MacRae, C. M., Mumme, W. G., Boer, S., Kampf, A. R., and Gable, R. W.: Monoclinic pleysteinite and hochleitnerite from the Hagendorf Süd pegmatite. Synchrotron microfocus diffraction studies on paulkerrite-group minerals, Can. J. Mineral. Petrol., 62, 513–527, 2024.

Sejkora, J., Skoda, R., Ondrus, P., Beran, P., and Susser, C.: Mineralogy of phosphate accumulations in the Huber stock, Krasno ore district, Slavkovsky les area, Czech Republic, J. Czech Geol. Soc., 51, 103–147, 2006.

Sheldrick, G. M.: Crystal structure refinement with SHELXL, Acta Crystallogr. C, 71, 3–8, 2015.

Silva, F. L. R., Filho, A. A. A., Silva, M. B., Balzuweit, K., Bantignies, J.-L., Caetano, E. W. S., Moreira, R. L., Freire, V. N., and Righi, A.: Polarized Raman, FTIR, and DFT study of $Na_2Ti_3O_7$ microcrystals, J. Raman Spectrosc., 49, 535–548, 2018.

Tu, C.-S., Guo, A. R., Tao, R., Katiyar, R. S., Guo, R., and Bhalla, A. S.: Temperature dependent Raman scattering in $KTiOPO_4$ and $KTiOAsO_4$ single crystals, J. Appl. Phys., 79, 3235–3240, 1996.